

CHANDRA OBSERVATIONS OF SDSS J1004+4112: CONSTRAINTS ON THE LENSING CLUSTER AND ANOMALOUS X-RAY FLUX RATIOS OF THE QUADRUPLY IMAGED QUASAR

NAOMI OTA,¹ NAOHISA INADA,² MASAMUNE OGURI,³ KAZUHISA MITSUDA,⁴ GORDON T. RICHARDS,⁵ YASUSHI SUTO,⁶ W. N. BRANDT,⁷ FRANCISCO J. CASTANDER,⁸ RYUICHI FUJIMOTO,⁴ PATRICK B. HALL,⁹ CHARLES R. KEETON,¹⁰ ROBERT C. NICHOL,¹¹ DONALD P. SCHNEIDER,⁷ DANIEL E. EISENSTEIN,¹² JOSHUA A. FRIEMAN,¹³ AND EDWIN L. TURNER³

Submitted to ApJL

ABSTRACT

We present results from *Chandra* observations of SDSS J1004+4112, a strongly lensed quasar system with a maximum image separation of 15''. All four bright images of the quasar, as well as resolved X-ray emission originating from the lensing cluster, are clearly detected. The emission from the lensing cluster extends out to approximately 1.5''. We measure the bolometric X-ray luminosity and temperature of the lensing cluster to be 4.7×10^{44} erg s⁻¹ and 6.4 keV, consistent with the luminosity-temperature relation for distant clusters. The mass estimated from the X-ray observation shows excellent agreement with the mass derived from gravitational lensing. The X-ray flux ratios of the quasar images differ markedly from the optical flux ratios, and the combined X-ray spectrum of the images possesses an unusually strong Fe K α emission line, both of which are indicative of microlensing.

Subject headings: galaxies: clusters: general — gravitational lensing — quasars: individual (SDSS J100434.91+411242.8) — X-rays: galaxies

1. INTRODUCTION

The quadruply lensed quasar SDSS J1004+4112, first identified as a gravitational lens candidate from optical imaging and spectroscopy from the Sloan Digital Sky Survey (SDSS; York et al. 2000), has an exceptionally large image separation of $\sim 15''$ (Inada et al. 2003; Oguri et al. 2004). The $z = 1.734$ quasar is multiply imaged by a cluster of galaxies (rather than a galaxy) at $z = 0.68$. This is the only known quasar strongly lensed by a central part of a massive cluster. The quasar appears to be radio-quiet since it is not detected in radio surveys such as the FIRST survey (Becker et al. 1995). Subsequent observations revealed additional intriguing aspects of the system. Microlensing of the broad emission line region

was discovered by a spectroscopic monitoring program (Richards et al. 2004). *Hubble Space Telescope* images detected the fifth image (Inada et al. 2005) and multiply imaged background galaxies (Sharon et al. 2005). SDSS J1004+4112 appears to be an ideal laboratory for exploration of the structure of a large cluster of galaxies and a quasar.

The uniqueness of SDSS J1004+4112 affords advantages that strongly argue for multiwavelength observations, of which X-ray observations constitute an essential part. Measurement of the X-ray properties of the lensing cluster offers an opportunity to improve lens models of SDSS J1004+4112. Moreover, the lensing cluster is the first example of a *strong-lens selected* cluster; it is interesting to determine if the cluster follows the empirical scaling relations between luminosities, temperatures, and masses. Second, we can investigate the magnification ratios of the quasar images at X-ray wavelengths, which may aid the interpretation of the microlensing event that has been observed at optical wavelengths (Richards et al. 2004). Indeed, X-ray flux ratios of lensed quasars are frequently different from optical flux ratios; this phenomenon has been attributed to microlensing (Chartas et al. 2004; Blackburne et al. 2006).

In this *Letter*, we report our analysis of an observation of SDSS J1004+4112 with the *Chandra X-Ray Observatory*. A key feature of *Chandra* images is the high angular resolution (on the order of 1''); this resolution is required to allow reliable separation of the X-ray flux of the lensing cluster from that of the quadruply imaged quasar. In this paper we will adopt a cosmological model with the matter density $\Omega_M = 0.27$, the cosmological constant $\Omega_\Lambda = 0.73$, and the Hubble constant $H_0 = 70 \text{ km s}^{-1} \text{Mpc}^{-1}$ (Spergel et al. 2003). At the redshift of the cluster ($z = 0.68$), 1'' corresponds to 7.16 kpc. Unless otherwise specified, quoted errors indicate the 90% confidence range.

2. OBSERVATIONS

¹ Cosmic Radiation Laboratory, RIKEN (The Institute of Physical and Chemical Research), 2-1 Hirosawa, Wako, Saitama 351-0198, Japan.

² Institute of Astronomy, Faculty of Science, The University of Tokyo, 2-21-1 Osawa, Mitaka, Tokyo 181-0015, Japan.

³ Princeton University Observatory, Peyton Hall, Princeton, NJ 08544.

⁴ Institute of Space and Astronautical Science, Japan Aerospace Exploration Agency, 3-1-1 Yoshinodai, Sagamihara, Kanagawa 229-8510, Japan.

⁵ Department of Physics and Astronomy, Johns Hopkins University, 3701 San Martin Drive, Baltimore, MD 21218.

⁶ Department of Physics, University of Tokyo, 7-3-1 Hongo, Bunkyo, Tokyo 113-0033, Japan.

⁷ Department of Astronomy and Astrophysics, Pennsylvania State University, 525 Davey Laboratory, University Park, PA 16802.

⁸ Institut d'Estudis Espacials de Catalunya/CSIC, Gran Capita 2-4, E-08034 Barcelona, Spain.

⁹ Department of Physics and Astronomy, York University, 4700 Keele Street, Toronto, Ontario, M3J 1P3, Canada.

¹⁰ Department of Physics and Astronomy, Rutgers University, 136 Frelinghuysen Road, Piscataway, NJ 08854.

¹¹ Institute of Cosmology and Gravitation (ICG), University of Portsmouth, Portsmouth, PO1 2EG, UK.

¹² Steward Observatory, University of Arizona, 933 North Cherry Avenue, Tucson, AZ 85721.

¹³ Astronomy and Astrophysics Department, University of Chicago, 5640 South Ellis Avenue, Chicago, IL 60637.

SDSS J1004+4112 was observed for 80 ks with the *Chandra* Advanced CCD Imaging Spectrometer (ACIS; Garmire et al. 2003) on 2005 January 1 and 2. The data were obtained with the ACIS S3 CCD operating in VFAINT mode. This CCD has a 1024×1024 pixel format with an image scale of $0''.492$ pixel $^{-1}$. The target was offset from the nominal aim point with a Y-offset of $-1'$, however, this has little effect on the spatial resolution. The CCD temperature during the observations was -120°C .

The data were processed using the standard software packages **CIAO 3.2.1** and **CALDB 3.0.3**. In the analysis of diffuse emission from the cluster (§3), periods of high background rates (defined by $> 20\%$ higher than the quiescent rates in the 2.5–7 keV band) were removed; the net exposure time is 62042 s. On the other hand, the data without lightcurve-filtering (79987 s) are used in the analysis of quasar components (§4) since the background counting rate is negligibly small for point sources.

The full band (0.5–7 keV) ACIS image is shown in Figure 1. The four images of SDSS J1004+4112 are clearly detected and resolved. The measured coordinates of the four X-ray quasar images are consistent with those obtained with *Subaru* (Oguri et al. 2004) within the positional accuracy of *Chandra* ($\lesssim 0''.4$). In addition, extended emission, roughly centered on the quasar images and extending out to $r \sim 1''.5$, is seen in the X-ray data. This component should arise from hot gas in the lensing cluster. The relative offsets of the coordinates of image A and the peak of the diffuse emission are (ΔRA , ΔDec) = $(-7''.4 \pm 1''.0, 4''.7 \pm 1''.0)$; the location of the peak of the extended emission is consistent with the position of the brightest cluster galaxy G1.

In the ACIS-S3 field, 39 point-like sources including the four quasar images were detected with the **wavdetect** algorithm with a significance threshold parameter of 10^{-6} . The bright source at (10:04:34.294, +41:12:20.22) with an X-ray flux of $\sim 1.0 \times 10^{-13}$ erg s $^{-1}$ cm $^{-2}$ (0.5–7 keV) has been observed serendipitously as part of the follow-up program to spectroscopically monitor components A and B at APO (Richards et al. 2004); a low S/N spectrum indicates a redshift of $z \sim 1.26$, which is marginally consistent with the second most likely photometric redshift ($z = 1.325$ with 26% confidence). The power-law slope, α_{ox} , connecting the rest frame 2500Å and 2 keV flux densities, is ~ -1.2 , which is roughly consistent with the α_{ox} -UV luminosity relation of AGNs (Strateva et al. 2005). The source at (10:04:33.684, +41:13:07.13) has an X-ray counting rate of $(4.4 \pm 0.7) \times 10^{-4}$ counts s $^{-1}$, and it is not a counter lens image of the Southern bright source as the separation angle is too large.

3. LENSING CLUSTER

3.1. Spectral Analysis

We derive the spectrum of the cluster component by extracting the data from the circular region within a radius of $1'$ that is centered on the position of the galaxy G1. The fluxes from the four quasar images and several additional point sources were removed from the spectral integration area by excluding all regions within a radius 10 times the size of the point spread function (PSF) at the source positions. The background was estimated from the data in a surrounding annulus ($1.5' < r < 2.5'$).

The source and background counts within $r < 1'$ are 1620 ± 52 and 914 ± 15 , respectively. The 0.5–7 keV extracted spectrum is fitted with the MEKAL thin-thermal plasma model (Mewe et al. 1985, 1986; Kaastra 1992; Liedahl et al. 1995) utilizing the **XSPEC** version 11. In this exercise, the Galactic hydrogen column density is fixed to $N_{\text{H}} = 1.13 \times 10^{20}$ cm $^{-2}$ (Dickey & Lockman 1990). The X-ray temperature is constrained to be $kT = 6.4_{-1.3}^{+2.1}$ keV and the metal abundance to be $Z = 0.26Z_{\odot}$ (the 90% upper limit is $0.65Z_{\odot}$). The Galactic absorption-corrected, 0.5–7 keV flux is 1.62×10^{-13} erg s $^{-1}$ cm $^{-2}$ ($r < 1'$). The bolometric X-ray luminosity within r_{500} is estimated as $L_{\text{X}} = 4.7 \times 10^{44}$ erg s $^{-1}$, where r_{500} is defined as the radius within which the average matter density is equal to $\Delta_c = 500$ times the critical density of the Universe at the cluster redshift. The β -model analysis in § 3.2 yields $r_{500} = 0.79$ Mpc. This luminosity is lower than the mean value expected from the luminosity-temperature relation of distant clusters, $L_{\text{X}} = 1.9_{-1.2}^{+2.4} \times 10^{45}$ erg s $^{-1}$ (Ota et al. 2006), but our estimated value is within the observed scatter of the data. The reduced chi-square of the best-fit model is $\chi^2/\text{dof} = 31.4/42$.

To investigate the radial temperature profile, we further analyzed spectra integrated from the inner $r < 0''.23$ (~ 100 kpc) region and the outer $0''.23 < r < 1'$ region of the lensing cluster. The fitted temperatures are $kT = 6.3_{-1.7}^{+2.5}$ keV and $5.9_{-1.5}^{+3.4}$ keV, respectively. These results suggest that there is not a strong temperature drop towards the cluster center, indicating radiative cooling is not important in this cluster.

3.2. X-ray Surface Brightness Profile

The one-dimensional radial surface-brightness profile of the extended X-ray emission was constructed by adopting a center at G1 and azimuthally averaging the 0.5–5 keV image, which was corrected for the telescope's vignetting and the detector responses and rebinned by a factor of two (i.e., 1 processed image pixel is $0''.98$). The radial profile was fit with the following two models: (1) the conventional β -model $S(r) = S_0[1 + (r/r_c)^2]^{-3\beta+1/2}$, and (2) the profile derived from the universal mass profile proposed by Navarro et al. (1997) plus isothermality of the cluster (Suto et al. 1998, hereafter NFW-SSM). The background was set to a constant in the fitting. We find that both models can fit the observed radial profile reasonably well: The reduced chi-square is $\chi^2/\text{dof} = 213.2/196$ and $205.5/196$ for the β -model and NFW-SSM model, respectively. The fitted values of the β -model parameters are $\beta = 0.59_{-0.04}^{+0.05}$ and $r_c = 9.7_{-1.7}^{+2.0}$ arcsec ($= 69_{-13}^{+15}$ kpc), while the NFW-SSM model results in $B = 9.1_{-0.8}^{+1.2}$ and $r_s = 39_{-9}^{+12}$ arcsec ($= 278_{-62}^{+85}$ kpc). The profile of the intra-cluster medium (ICM) has a compact core, typical of observed surface brightness profiles of relaxed clusters.

The fit shows excess flux in the measurements compared to the models within $r \lesssim 20$ kpc. This is often seen in central regions of relaxed clusters (e.g., Mohr, Mathiesen & Evrard 1999). Since the central emission is significantly extended compared with the PSF and the hardness ratio is consistent with $kT \sim 4$ keV thermal emission, we ascribe the excess X-ray flux to a hot ICM rather than the galaxy G1 or a point source. X-ray emis-

sion from the central fifth image (Inada et al. 2005) is unlikely: the contribution is estimated to be only $\sim 3 - 9$ counts (i.e., about 5 – 15% of the central $r < 2''$ emission) assuming that the X-ray emission from the fifth image has similar intensity ratios as those measured in the HST ACS image. The observed profile may be better fitted by introducing the two-component β -models or increasing the inner slope parameter α in the NFW-SSM model; however, we will not pursue this process further since the above two models already provided acceptable fits to the data. A considerably deeper observation is needed to constrain further the gas profile in the innermost region.

From the image analysis, the extent of the X-ray emission above the 3σ background level is found to be $r_X = 91''$ (= 652 kpc), which is close to an overdensity radius of $r_{500} = 0.79^{+0.15}_{-0.11}$ Mpc.

3.3. Cluster Mass Distribution

Under the assumption of hydrostatic equilibrium, we can infer the mass distribution of the lensing cluster from the X-ray temperature and surface-brightness profiles. Because there is not a significant radial dependence of the X-ray temperature in the observations, we assume isothermality of the gas in the mass estimation. Figure 2 shows the cylindrical cluster mass projected within a radius r derived from each surface mass distribution profile. We find that both models yield consistent mass profiles within the measurement errors.

It is interesting to compare the mass derived from X-ray analysis with that from gravitational lensing. Williams & Saha (2004) derived the cylindrical mass to be $M(< 100 \text{ kpc}) = (5 \pm 1) \times 10^{13} M_\odot$, and Sharon et al. (2005) estimated $M(< 110 \text{ kpc}) = 6 \times 10^{13} M_\odot$. From Figure 2, it is clear that both mass estimations are in excellent agreement with the mass profile from the X-ray observation. For instance, we find the cylindrical masses within 100 kpc for the β -model and NFW-SSM model are $5.2^{+1.8}_{-1.1} \times 10^{13} M_\odot$ and $5.0^{+1.6}_{-1.0} \times 10^{13} M_\odot$, respectively. The discrepancy between X-ray and lensing masses has been reported in many lensing clusters (e.g., Hattori et al. 1999), and is often ascribed to the projection of the extra matter along line-of-sight, the elongation of the lensing cluster along the line-of-sight direction, or a departure from equilibrium. The excellent agreement between X-ray and lensing masses implies that none of these effects is significant for SDSS J1004+4112.

For the NFW-SSM model and $\Delta_c = 18\pi^2\Omega^{0.427}$ (Nakamura & Suto 1997), the virial mass and the concentration parameter are constrained to be $M_{\text{vir}} = 6.0^{+3.4}_{-2.1} \times 10^{14} M_\odot$ and $c_{\text{vir}} = 6.1^{+1.5}_{-1.2}$. The value of the concentration parameter is slightly larger than the theoretically expected median value for this virial mass and redshift, $c_{\text{vir}} \sim 4.0$ (Bullock et al. 2001), but is within 2σ scatter among different clusters.

4. QUASAR IMAGES

4.1. Anomalous Flux Ratios

The observed source counts for the four images, A–D, are 1237, 1580, 1312, and 763, in the 0.5–7 keV band, respectively. Light curves were produced with time resolutions of 2048 or 4096 sec. We did not find any clear sign of time variability within the statistical uncertain-

ties. Note that each component was extracted using a circular region with a radius of $2''$ in the analysis presented in this section. The sum of the background and contamination from the cluster emission are estimated to be only $\sim 1\%$ of the source counts for A–C, and $\sim 3\%$ for D, and are negligibly small compared to the statistical errors of the source spectra.

We measure the energy fluxes of lensed images in the *Chandra* data by fitting each spectrum with a power-law plus Gaussian line model (see the next subsection for details). The results are summarized in Table 1. The X-ray flux ratios differ significantly from those measured in the optical. Since for fold lenses such as SDSS J1004+4112, the two images near the critical curve are usually brighter than the other two images and since the optical flux ratios were reproduced with simple mass models (Oguri et al. 2004), we believe that the X-ray, rather than the optical, ratios are “anomalous”. The optical/X-ray flux ratios of images C and D are almost the same, therefore the most natural interpretation is that the image A is demagnified by a factor of ~ 3 in X-rays. This interpretation is consistent with the observation that image A appears to be a saddle-point image (Oguri et al. 2004; Williams & Saha 2004) which is more likely to be demagnified by perturbations than the other images (Schechter & Wambsganss 2002).

In Table 1, we also show the values of α_{ox} to check the consistency of the X-ray and optical fluxes. Although the values are somewhat higher than the $\alpha = -1.33$ that is expected from the UV luminosity of SDSS J1004+4112 (assuming a magnification factor of 50 for image A) and the α_{ox} -UV luminosity relation (Strateva et al. 2005), they are within the scatter of the relation.

4.2. X-ray Spectrum

The spectrum of the lensed quasar component is displayed in Figure 3. To enhance the signal-to-noise ratio, the total spectrum (sum of the images A, B, C, and D) is plotted. A remarkable feature in the spectrum is a relatively strong emission line centered at 2.3 keV in our frame. We fit the spectrum with a power-law plus Gaussian line profile model (see Figure 3). In comparison to just a power-law model, the fit was improved at the $> 99.99\%$ confidence level according to the F-test ($\Delta\chi^2 = 35.9$ for three additional parameters). Again, the Galactic hydrogen column density is fixed to $N_{\text{H}} = 1.13 \times 10^{20} \text{ cm}^{-2}$ since we did not find meaningful intrinsic absorption. The fitting yields the power-law index $\Gamma = 1.90 \pm 0.04$, the centroid energy of the line $E = 6.32^{+0.15}_{-0.14}$ keV, and the Gaussian width of the line $\sigma = 355^{+128}_{-169}$ eV. The line centroid is consistent with the neutral iron $\text{K}\alpha$ line at 6.4 keV in the quasar rest frame and the derived σ suggests that the line is intrinsically broad. From the result, we can compute the equivalent width $\text{EW} = 738^{+236}_{-227}$ eV in the quasar rest frame. The luminosity is $4.8 \times 10^{45} \text{ erg s}^{-1}$ in the 2–10 keV band. The reduced chi-square of the best fit model is $\chi^2/\text{dof} = 108.1/112$.

There is a well-known negative correlation between the strength of the iron line and the X-ray luminosity in quasars (e.g., Nandra et al. 1997). The derived equivalent width is larger by a factor of ~ 3 than that expected from the relation of Nandra et al. (1997) and a factor

of $\gtrsim 4$ than that from recent *XMM-Newton* observations (Page et al. 2004; Jiménez-Bailón et al. 2005). Combined with the result in §4.1, we speculate that microlensing de-magnifies the X-ray continuum of image A, while keeping (or amplifying) the Fe $K\alpha$ line. Moreover, microlensing of emission lines in the optical band has been detected for this lens system (Richards et al. 2004), providing additional evidence for the microlensing hypothesis.

The origin of the strong Fe $K\alpha$ line is further explored by fitting the spectrum of each image, rather than the sum of all images, where the centroid energy and the width of the line are fixed to the best-fit value derived above. The result is summarized in Table 1. Although the errors are very large, the Fe $K\alpha$ line is detected most significantly for image A, supporting the interpretation above. We also find that the hardness ratios of the images are marginally consistent with each other (see Table 1).

We note that from the Keck/LRIS spectroscopy of C IV absorption lines (Oguri et al. 2004), the A-B difference spectrum resembles that of the troughs seen in a broad absorption line (BAL) quasar. However, these features appear to result from excess *emission* in component A rather than absorption in component B. In addition, BAL quasars are generally X-ray faint due to a large intrinsic absorption ($N_{\text{H}} \sim 10^{22-23} \text{ cm}^{-2}$; e.g., Green et al. 2001; Gallagher et al. 2002) and tend to show a very negative α_{ox} ($\alpha_{\text{ox}} < -1.8$; Green et al. 2001). The α_{ox} values for SDSS J1004+4112 are inconsistent with those of BAL quasars. While we have shown that the image A is fainter than B in X-ray (Table 1), our analysis also indicates that the absorbed power-law model cannot reproduce the different X-ray spectra of A and B and the

optical flux ratio between A and B, simultaneously. From the above multiple independent indications, we suggest that the microlensing phenomenon is the most natural interpretation for the present data.

5. SUMMARY

We have presented results from *Chandra* observations of SDSS J1004+4112, a large-separation gravitational lens system created by a cluster of galaxies. We have detected X-ray emission from the lensing cluster as well as four lensed quasar images.

From the cluster X-ray emission, we have constrained the bolometric luminosity and the temperature to be $L_{\text{X}} = 4.7 \times 10^{44} \text{ erg s}^{-1}$ and $kT = 6.4_{-1.3}^{+2.1} \text{ keV}$, consistent with the luminosity-temperature relation of distant clusters. We have reconstructed the mass profile of the lensing cluster assuming isothermality and hydrostatic equilibrium, and found that the mass within 100 kpc excellently agrees with that expected from strong lensing.

X-ray emission from the lensed quasar images displays two anomalies: the presence of a strong Fe $K\alpha$ line and significant differences in the flux ratios from those found in the optical band. Both of these features are suggestive of microlensing. The idea is supported by the fact that image A, which appears most anomalous, is a saddle-point image.

We are grateful to A. Yonehara for useful discussions. N.O. acknowledges support from the Special Postdoctoral Researchers Program of RIKEN.

REFERENCES

Becker, R. H., White, R. L., & Helfand, D. J. 1995, ApJ, 450, 559
 Blackburne, J. A., Pooley, D., & Rappaport, S. 2006, ApJ, in press (astro-ph/0509027)
 Bullock, J. S., Kolatt, T. S., Sigad, Y., Somerville, R. S., Kravtsov, A. V., Klypin, A. A., Primack, J. R., & Dekel, A. 2001, MNRAS, 321, 559
 Chartas, G., Eracleous, M., Agol, E., & Gallagher, S. C. 2004, ApJ, 606, 78
 Dickey, J. M., & Lockman, F. J. 1990, ARA&A, 28, 215
 Gallagher, S. C., Brandt, W. N., Chartas, G., & Garmire, G. P. 2002, ApJ, 567, 37
 Garmire, G.P., Bautz, M.W., Ford, P.G., Nousek, J.A., & Ricker, G.R. 2003, Proc.SPIE, 4851, 28
 Green, P. J., Aldcroft, T. L., Mathur, S., Wilkes, B. J., & Elvis, M. 2001, ApJ, 558, 109
 Hattori, M., Kneib, J., & Makino, N. 1999, Progress of Theoretical Physics Supplement, 133, 1
 Inada, N., et al. 2003, Nature, 426, 810
 Inada, N., et al. 2005, PASJ, 57, L7
 Jiménez-Bailón, E., Piconcelli, E., Guainazzi, M., Schartel, N., Rodriguez-Pascual, P. M., & Santos-Lleó, M. 2005, A&A, 435, 449
 Kaastra, J.S. 1992, An X-Ray Spectral Code for Optically Thin Plasmas
 Liedahl, D.A., Osterheld, A.L., and Goldstein, W.H. 1995, ApJ, 438, L115
 Mewe, R., Gronenschield, E.H.B.M., and van den Oord, G.H.J. 1985, A&AS, 62, 197
 Mewe, R., Lemen, J.R., & van den Oord, G.H.J. 1986, A&AS, 65, 511
 Mohr, J. J., Mathiesen, B., & Evrard, A. E. 1999, ApJ, 517, 627
 Nakamura, T. T., & Suto, Y. 1997, Prog. Theor. Phys., 97, 49
 Nandra, K., George, I. M., Mushotzky, R. F., Turner, T. J., & Yaqoob, T. 1997, ApJ, 488, L91
 Navarro, J. F., Frenk, C. S., & White, S. D. M. 1997, ApJ, 490, 493
 Oguri, M., et al. 2004, ApJ, 605, 78
 Ota, N., Kitayama, T., Masai, K., & Mitsuda, K. 2006, ApJ, in press (astro-ph/0512180)
 Page, K. L., O'Brien, P. T., Reeves, J. N., & Turner, M. J. L. 2004, MNRAS, 347, 316
 Richards, G. T., et al. 2004, ApJ, 610, 679
 Schechter, P. L., & Wambsganss, J. 2002, ApJ, 580, 685
 Sharon, K., et al. 2005, ApJ, 629, L73
 Spergel, D.N., et al. 2003, ApJS, 148, 1
 Strateva, I. V., Brandt, W. N., Schneider, D. P., Vanden Berk, D. G., & Vignali, C. 2005, AJ, 130, 387
 Suto, Y., Sasaki, S., & Makino, N. 1998, ApJ, 509, 544
 Williams, L. L. R., & Saha, P. 2004, AJ, 128, 2631
 York, D.G., et al. 2000, AJ, 120, 1579

TABLE 1
X-RAY AND OPTICAL PROPERTIES OF SDSS J1004+4112

| Name | F_X^a | hardness ^b | F_{opt}^c | F_{opt}/F_X | α_{ox} | EW [eV] ^d |
|------|-----------------|-----------------------|--------------------|----------------------|----------------------|----------------------|
| A | 0.95 ± 0.03 | 0.30 ± 0.02 | 1.00 | 1.00 | -1.22 ± 0.01 | 1151^{+374}_{-554} |
| B | 1.21 ± 0.03 | 0.26 ± 0.02 | 0.73 | 0.58 | -1.11 ± 0.01 | 593^{+284}_{-446} |
| C | 1.01 ± 0.03 | 0.27 ± 0.02 | 0.35 | 0.33 | -1.07 ± 0.01 | 842^{+443}_{-389} |
| D | 0.56 ± 0.02 | 0.34 ± 0.03 | 0.21 | 0.35 | -1.05 ± 0.01 | 552^{+369}_{-268} |

^aAbsorption-corrected, 0.5–7 keV X-ray flux in units of $10^{-13}\text{erg s}^{-1}\text{cm}^{-2}$ and the 1- σ error.

^bHardness ratios defined by the count rate ratios in 2 – 7 keV and 0.5 – 2 keV bands. Errors indicate 68% confidence limits.

^cFlux normalized by the flux of image A in the HST F814W image (Inada et al. 2005). Measurement errors are negligibly small.

^dEquivalent width of the Fe K α line in the quasar rest frame.

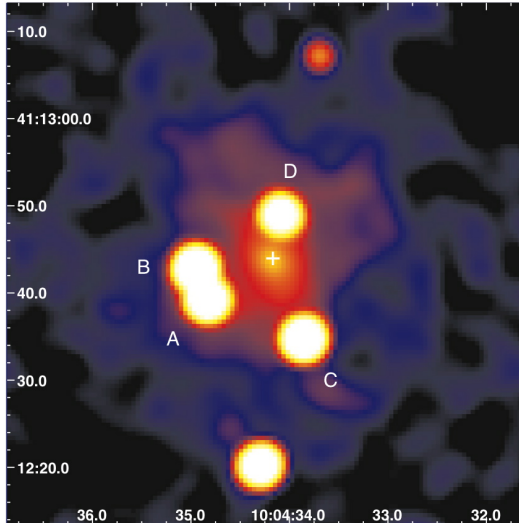


FIG. 1.— Adaptively-smoothed ACIS-S3 image of SDSS J1004+4112 in the 0.5–7 keV band. Both multiple images of SDSS J1004+4112, A–D, and the extended emission from the lensing cluster (whose X-ray peak is marked with the cross) are clearly seen. The images A and B, which have a minimum angular separation of $3''.8$, are also resolved in the raw image. The point source at (10:04:34.294, +41:12:20.22) is a quasar (see text).

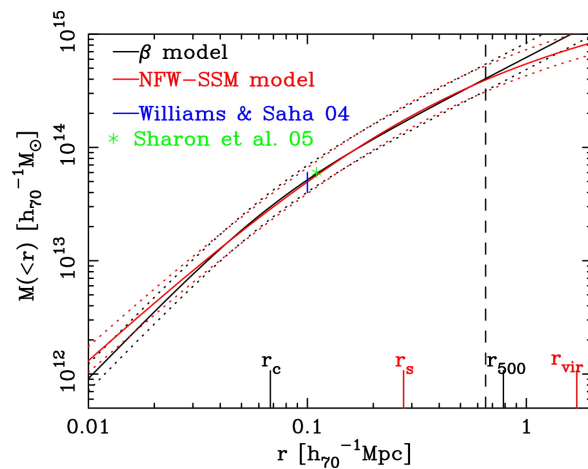


FIG. 2.— Enclosed mass of the lensing cluster, M_X , for the β -model (black) and the NFW-SSM model (red). The dotted lines indicate the 90% error ranges. Note that M_X is a cylindrical cluster mass projected within a radius r . The masses derived from gravitational lensing (Williams & Saha 2004; Sharon et al. 2005) are also shown for comparison. The vertical dashed line shows the extent of the diffuse X-ray emission, r_X (see text).

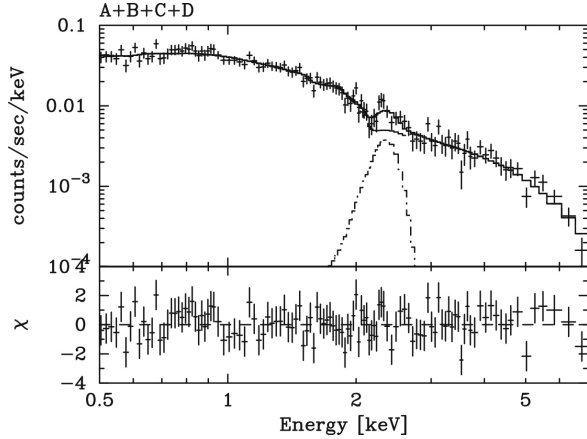


FIG. 3.— Total quasar spectrum (the sum of images A, B, C, and D) fit with a power-law (*dashed*) plus Gaussian (*dot-dashed*) model, which is shown by the solid line.